Editors' Suggestion

Topological Singularity Induced Chiral Kohn Anomaly in a Weyl Semimetal

Thanh Nguyen,[1,*] Fei Han,[1,*] Nina Andrejevic,[2,*] Ricardo Pablo-Pedro,[1,*] Anuj Apte,[3] Yoichiro Tsurimaki,[4] Zhiwei Ding,[2] Kunyan Zhang,[5] Ahmet Alatas,[6] Ercan E. Alp,[6] Songxue Chi,[7] Jaime Fernandez-Baca,[7] Masaaki Matsuda,[7] David Alan Tennant,[7] Yang Zhao,[8,9] Zhijun Xu,[8,9] Jeffrey W. Lynn,[8] Shengxi Huang,[5] and Mingda Li[1,†]

[1]*Department of Nuclear Science and Engineering, MIT, Cambridge, Massachusetts 02139, USA*
[2]*Department of Materials Science and Engineering, MIT, Cambridge, Massachusetts 02139, USA*
[3]*Department of Physics, MIT, Cambridge, Massachusetts 02139, USA*
[4]*Department of Mechanical Engineering, MIT, Cambridge, Massachusetts 02139, USA*
[5]*Department of Electrical Engineering, The Pennsylvania State University, University Park, Pennsylvania 16802, USA*
[6]*Advanced Photon Source, Argonne National Laboratory, Lemont, Illinois 60439, USA*
[7]*Neutron Scattering Division, Oak Ridge National Laboratory, Oak Ridge, Tennessee 37831, USA*
[8]*NIST Center for Neutron Research, National Institute of Standards and Technology, Gaithersburg, Maryland 20899, USA*
[9]*Department of Materials Science and Engineering, University of Maryland, College Park, Maryland 20742, USA*

(Received 23 March 2020; accepted 13 May 2020; published 11 June 2020)

The electron-phonon interaction (EPI) is instrumental in a wide variety of phenomena in solid-state physics, such as electrical resistivity in metals, carrier mobility, optical transition, and polaron effects in semiconductors, lifetime of hot carriers, transition temperature in BCS superconductors, and even spin relaxation in diamond nitrogen-vacancy centers for quantum information processing. However, due to the weak EPI strength, most phenomena have focused on electronic properties rather than on phonon properties. One prominent exception is the Kohn anomaly, where phonon softening can emerge when the phonon wave vector nests the Fermi surface of metals. Here we report a new class of Kohn anomaly in a topological Weyl semimetal (WSM), predicted by field-theoretical calculations, and experimentally observed through inelastic x-ray and neutron scattering on WSM tantalum phosphide. Compared to the conventional Kohn anomaly, the Fermi surface in a WSM exhibits multiple topological singularities of Weyl nodes, leading to a distinct nesting condition with chiral selection, a power-law divergence, and non-negligible dynamical effects. Our work brings the concept of the Kohn anomaly into WSMs and sheds light on elucidating the EPI mechanism in emergent topological materials.

DOI: 10.1103/PhysRevLett.124.236401

In 1959, Walter Kohn proposed the anomalous phonon dispersion behavior in a metal, which arises when electrons lose their dielectric screening [1]. This anomaly, known as a Kohn anomaly, directly images the Fermi surface on the phonon dispersion, and overturned the long-held belief that the weak EPI can only lead to negligible effects on phonon properties. Intuitively, a Kohn anomaly occurs when electronic states $\boldsymbol{k}_1$ and $\boldsymbol{k}_2$ near the Fermi surface are parallelly nested by a phonon with wave vector $\boldsymbol{q} \equiv \boldsymbol{k}_2 - \boldsymbol{k}_1$. This is a stringent condition only met by a single $q \equiv |\boldsymbol{q}|$ value at $q \approx 2k_F$, where k_F is the Fermi wave vector. Extensive research has delved into the role of Kohn anomalies in conventional [2] and unconventional superconductors [3,4], carbon materials such as carbon nanotubes [5], graphene [6–8], and graphite [9], as well as other low-dimensional systems such as 1D conductors [10] and topological insulators [11].

The recent development of WSMs [12–16] offers a new platform to realize exotic phonon properties, such as the phonon Hall effect [17], chiral magnetic effect [18], and chiral anomaly in phonon spectra [19]. As such, WSMs could serve as an intriguing platform to study Kohn anomalies due to the presence of topologically protected Weyl nodes and 3D linear-dispersive Weyl fermions.

In this Letter, we theoretically predict and experimentally observe a new type of Kohn anomaly in WSM, which exhibits a few novel features. First, since the simply-connected Fermi surface in a conventional Fermi liquid evolves into disconnected topological singularities of chiral Weyl nodes, the condition to achieve Kohn anomalies becomes largely relaxed. As the EPI does not change chirality, it plays an essential role in understanding the coupling strength through the following requisite. For two Weyl nodes located at $\boldsymbol{k}_{W1}$ and $\boldsymbol{k}_{W2}$, both of which necessarily share the same chirality, a phonon with $\boldsymbol{q} \approx \boldsymbol{k}_{W2} - \boldsymbol{k}_{W1}$ can directly lead to the anomaly. In particular, for our chosen material of type-I WSM tantalum phosphide (TaP), which contains two sets of inequivalent Weyl nodes $\{\boldsymbol{k}_{W1}\}$ and $\{\boldsymbol{k}_{W2}\}$, there is a subset of nodes satisfying $\boldsymbol{k}_{W2} - \boldsymbol{k}_{W1} \in \{\boldsymbol{k}_{W2}\}$ [14]. As a result, phonon $\boldsymbol{q}$ values can

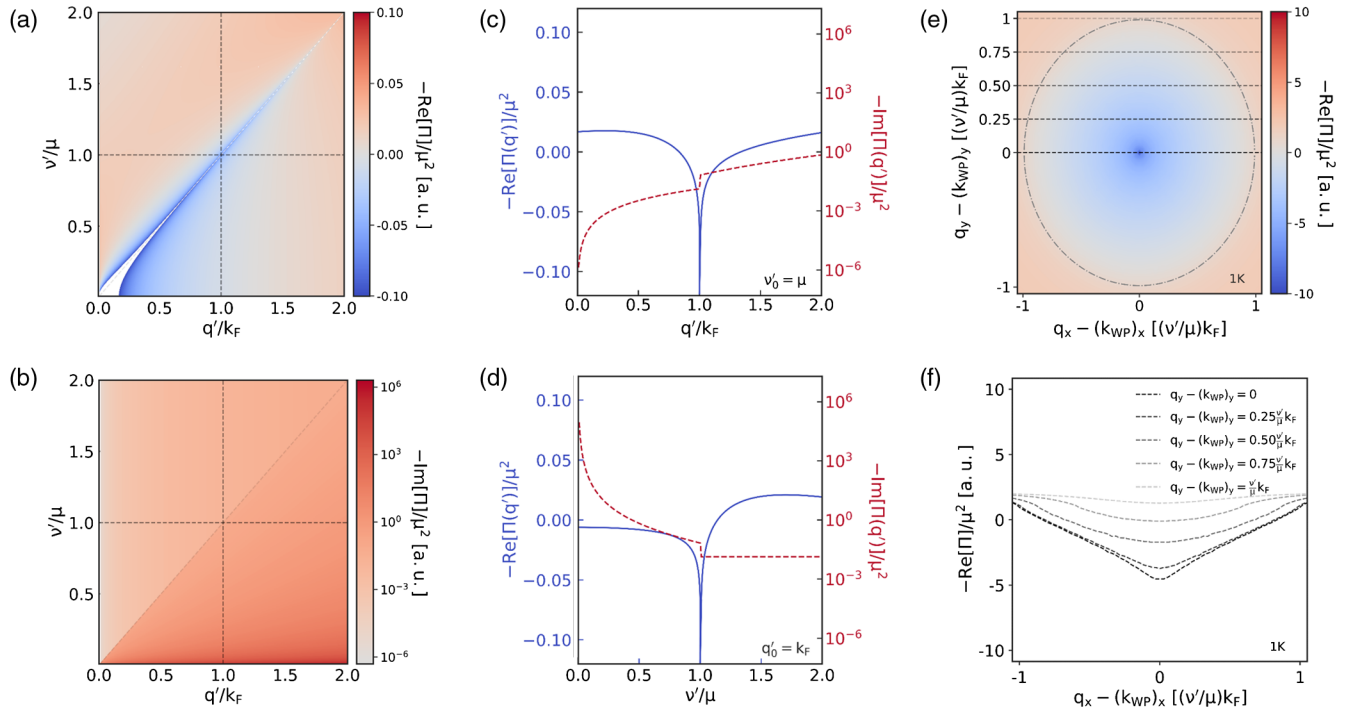

FIG. 1. Field-theoretical calculations of topological Kohn anomaly. Density plots of the (a), real, and the (b), imaginary part of the polarization function $-\Pi(\boldsymbol{q}', \nu')$ at $T = 1$ K. (c) Constant-frequency line profile of $-\mathrm{Re}[\Pi(\boldsymbol{q}', \nu'_0 = \mu)]$ and $-\mathrm{Im}[\Pi(\boldsymbol{q}', \nu'_0 = \mu)]$. (d) Constant-wave vector line profile of $-\mathrm{Re}[\Pi(q'_0 = k_F, \nu')]$ and $-\mathrm{Im}[\Pi(q'_0 = k_F, \nu')]$. (e) Density plot of $-\mathrm{Re}[\Pi(\boldsymbol{q_x} - \boldsymbol{k}_{\mathrm{WP}_x}, \boldsymbol{q_y} - \boldsymbol{k}_{\mathrm{WP}_y})]$, which represents a realistic experimental setup scanning near the Weyl node. (f) Line cuts at different values of deviations away from a Weyl node. There is a noticeable dip at the Weyl node, yet even away from the Weyl nodes, softening can still exist due to the pointlike Weyl node and dynamic effect.

be chosen directly at Weyl nodes. Second, instead of a logarithmic divergence as in a Fermi liquid or a weak power-law divergence as in graphene [20], the Kohn anomaly in a WSM shows a stronger power-law divergence. This counterintuitive result originates from the 3D dispersion. Third, in a WSM, the Debye frequency ω_D can be higher than the Fermi level E_F, indicating a nonnegligible dynamical effect, since the frequency dependence of the dielectric function occurs on the scale of ω_D. Such a dynamical effect leads to softening within a finite regime in the Brillouin zone instead of at an individual $\boldsymbol{q}$ point. This contrasts with the conventional Fermi liquid, where static screening suffices since $\omega_D \ll E_F$. Our work represents the first reported observation of a Kohn anomaly in a topological nodal semimetal, and offers a new tool for probing the EPI characteristics in a broader category of topological materials.

Field-theoretical calculation of topological Kohn anomaly.—The dielectric screening from internode scattering via a phonon $\boldsymbol{q} = \boldsymbol{k}_{W2} - \boldsymbol{k}_{W1}$ is computed for 3D linear dispersive Weyl fermions using $E(\boldsymbol{k}) = \pm v_F|\boldsymbol{k} - \boldsymbol{k}_{Wj}| - \mu_j$, where v_F is the Fermi velocity and $j = 1, 2$ denotes different Weyl nodes at chemical potential μ_j. The polarization operator $\Pi(\nu, \boldsymbol{q})$ from the inter-Weyl-node scattering can be written as (see Supplemental Material A [21]):

$$\Pi(\nu, \boldsymbol{q}) \approx -\frac{(v_F q')^2}{24\pi^2}\left(\ln\left|\frac{4(v_F\Lambda)^2}{(v_F q')^2 - \nu'^2}\right| + \frac{(v_F q')^2 - \nu'^2}{10(v_F\Lambda)^2} - \frac{1}{3}\right), \tag{1}$$

where $q' = |\boldsymbol{q} + \boldsymbol{k}_{W1} - \boldsymbol{k}_{W2}|$, $\nu' = \nu - \mu_1 + \mu_2$ and Λ is a momentum cutoff. Since the dynamical dielectric function $\epsilon_r(\nu, \boldsymbol{q})$ can be written as $\epsilon_r(\nu, \boldsymbol{q}) = 1 - 4\pi e^2\Pi(\nu, \boldsymbol{q})/(\kappa q^2)$, we see immediately that a Kohn anomaly with a strong power-law divergence can occur by satisfying the following condition,

$$v_F q' = \pm\nu', \tag{2}$$

whereupon the momentum derivative of the dielectric function diverges:

$$\frac{\partial\varepsilon_r}{\partial q} \propto \frac{(v_F q')^3}{(v_F q')^2 - (\nu')^2}. \tag{3}$$

The divergence condition for a Kohn anomaly implies that the momentum mismatch $\delta\boldsymbol{q} \equiv \boldsymbol{q} - (\boldsymbol{k}_{W2} - \boldsymbol{k}_{W1})$ can be compensated by a finite dynamical effect ν'. Consequentially, a patch of $\boldsymbol{q}$ values in momentum space with small momentum mismatch can still experience a Kohn anomaly. In fact, the simple divergence condition $v_F q' = \pm\nu'$ will persist even with finite doping. The density

plots of the real and imaginary parts of $-\Pi(\nu, \boldsymbol{q})$ at finite doping and temperature are shown in Figs. 1(a) and 1(b) (additional temperatures in Figs. S1 and S2 in Ref. [21]). The divergence appears as a sharp peak along the line $v_F q' = \nu'$, and is further visualized along constant-frequency $\nu'_0/\mu = 1$ and constant-wave vector $q'_0/k_F = 1$ cuts in Figs. 1(c) and 1(d), respectively, in reduced dimensionless units, where $\mu \equiv \sqrt{\mu_1^2 + \mu_2^2}$, and $k_F \equiv \mu/v_F$. Figure 1(e) is a plot of $-\mathrm{Re}[\Pi(\nu, \boldsymbol{q})]$ in $\delta\boldsymbol{q}_x$–$\delta\boldsymbol{q}_y$ space integrated from 0 to ν', which is proportional to the magnitude of the phonon softening and reveals a negative contribution emanating from the zero-mismatch condition as a result of the divergence at $v_F q' = \pm\nu'$. The divergence is alleviated here by a small numerical imaginary part mimicking the considerations of additional scattering terms. Line cuts in $\delta\boldsymbol{q}_x$–$\delta\boldsymbol{q}_y$ space shown in Fig. 1(f) reveal a broad dip in $-\mathrm{Re}[\Pi(\nu, \boldsymbol{q})]$ that does not necessarily occur at the zero-mismatch condition, thereby demonstrating the existence of a non-negligible dynamical effect. It is worthwhile mentioning that although the polarization in Figs. 1(c) and 1(d) show a sharp divergence, the distinct condition to fulfill a Kohn anomaly in a patch of $\boldsymbol{q}$ values eventually leads to a broad "bowl-shaped" softening in the Brillouin zone, which qualitatively agrees well with the experiments without knowing the EPI coupling constants. The EPI, embodied through an expression for $\Pi(\nu, \boldsymbol{q})$ characteristic of WSMs, results in a distinct renormalization of the bare ionic phonon frequencies within a range of $\boldsymbol{q}$ space conducive to a different nature of Kohn anomaly.

Phonon dispersion along high-symmetry directions.—TaP crystallizes in the body-centered tetragonal space group $I4_1md$ (109) [Fig. 2(a)] and hosts two sets of inequivalent Weyl nodes, denoted W1 and W2 [Fig. 2(b)]. We first present the phonon dispersion measurements of a TaP crystal (Fig. S3, Supplemental Material B and C [21]) along a high-symmetry loop Γ-Σ-Σ_1-Z-Γ [Fig. 2(c) with data in Fig. S4] using inelastic x-ray scattering (IXS). We focused on the low-energy phonons (< 25 meV), which include the Ta optical phonons but not those associated with the motion of P atoms. The phonon energies are extracted using damped harmonic oscillator models to convolute with the instrument resolution functions, and then fitting the measured spectra. The resulting phonon dispersion is shown in Fig. 2(d) (and Fig. S6 [21] for lower temperatures), along which the intensity of fitting the intrinsic scattering (after deconvolution) is plotted as a color map. Gray lines designate *ab initio* phonon dispersion calculations for which the procedure is detailed in Supplemental Material D [21]. Further data were collected using inelastic neutron scattering (INS), which agree well with the dispersion from IXS (Fig. S7 [21]). The excellent agreement between experiments and *ab initio* calculations indicates a level of reliability of computational phonon spectra, which serves as a basis to compare phonon dispersions away from high-symmetry lines.

Observation of topological chiral Kohn anomaly.—We present experimental signatures highlighting the presence

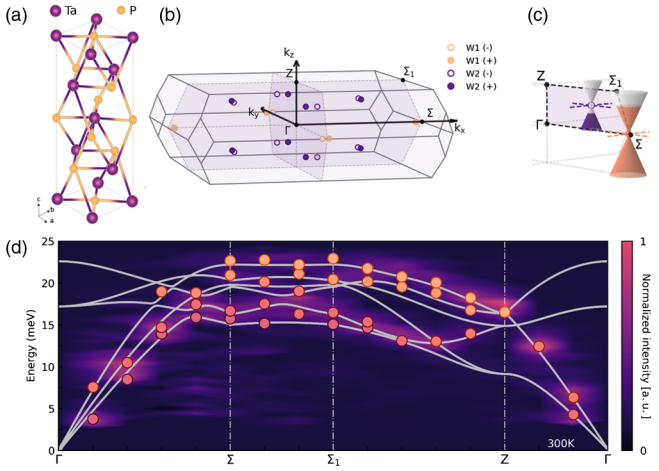

FIG. 2. Phonon dispersion of TaP. (a) Crystal structure of TaP with (b), corresponding Brillouin zone which features the locations and Berry curvature signs of paired Weyl nodes W1 (orange) and W2 (purple). (c) Schematic of relative energy location of W1 and W2 Weyl nodes. (d) Low-energy phonon dispersion of TaP, measured by IXS and INS at 300 K along the high-symmetry loop Γ-Σ-Σ_1-Z-Γ. Points represent extracted phonon modes from measurements. The gray lines denote *ab initio* calculations showing excellent agreement, and the color map represents the spectra intensity.

of a Kohn anomaly at the W2 Weyl node, predicted in Fig. 1. In our TaP sample, the W1 Weyl nodes are ~60 meV below E_F, while W2 nodes are a few meV above E_F [Fig. 3(a)]. As a result, W1 represents a much larger carrier pocket than W2. We carried out IXS measurements at $\boldsymbol{q}$ values near a W2 Weyl node located at $\boldsymbol{k}_{W2'} = (0.271, 0.024, 0.578)$ (Fig. S8 [21]). Even without fitting, the phonon softening at the Weyl node can be seen clearly from the original data in Fig. 3(b). The bowl-shaped softening characteristics resemble the field-theoretical prediction in Fig. 1(f) very well, although a quantitative agreement is unpractical, requiring the mode-resolved EPI constants. The fitted phonon dispersion relation of the highest acoustic and the lowest optical phonons along the k_x and k_y directions within the plane containing $\boldsymbol{k}_{W2'}$ are shown in Figs. 3(c)–3(f). Strong phonon softening is observed at both $T = 18$ and $T = 300$ K, and in both the k_x and k_y directions. Such softening is absent in *ab initio* calculations without considering EPI. The semi-quantitative agreement between theory and experimental trends, the consistent softening behavior at multiple $\boldsymbol{q}$ points, and the absence of softening in *ab initio* calculations without EPI consideration, overall strongly suggest an EPI nature of the phonon softening. Additionally, the phonon softening takes place at all measured temperatures, indicating a possible topological robustness. Such softening can be understood as a Kohn anomaly from inter-Weyl node scattering. In fact, it is possible to nest a W1 electronic state at $\boldsymbol{k}_{W1} = (-0.518, -0.014, 0)$ with another W2 state $\boldsymbol{k}_{W2} = (-0.271, 0.024, 0.578)$, both with "+" chirality,

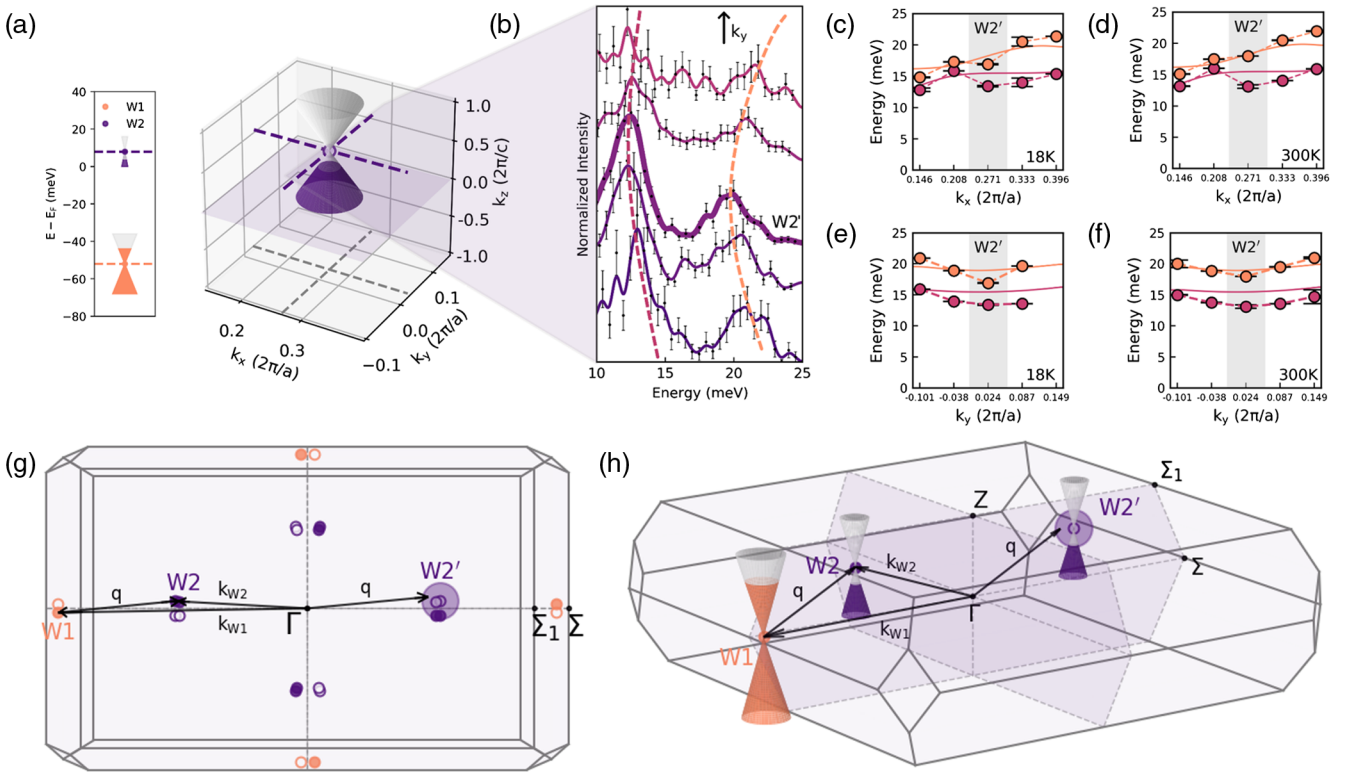

FIG. 3. Topological Kohn anomaly at W2 Weyl node. (a) Location of the W2 Weyl node in energy and momentum space. (b) Phonon spectra near the W2 Weyl node, with central thicker line denoting the location of W2′. Strong phonon softening at this Weyl node is observed. (c)–(f) Dispersion of two representative phonon modes near W2 at 18 and 300 K, along the k_x and k_y directions. Solid lines correspond to *ab initio* calculations without the EPI, where their discrepancy with experimental data further supports the strong softening near the W2 node. 2D (g) and 3D (h) showing the realization condition of Kohn anomaly, where a phonon $\boldsymbol{q} = \boldsymbol{k}_{W2} - \boldsymbol{k}_{W1} \approx \boldsymbol{k}_{W2'}$ connects two Weyl nodes $\boldsymbol{k}_{W1}$ and $\boldsymbol{k}_{W2}$.

via a phonon $\boldsymbol{q} = \boldsymbol{k}_{W2} - \boldsymbol{k}_{W1} \approx \boldsymbol{k}_{W2'}$, with a mismatch $|\boldsymbol{q} - \boldsymbol{k}_{W2'}|/|\boldsymbol{k}_{W2'}| \sim 4\%$. Details relating to different nesting combinations are listed in Supplemental Material E [21]. The schematics of this nesting condition are shown in Figs. 3(g)–3(h). As mentioned previously, the dynamical effect significantly reduces the mismatch and further enables the Kohn anomaly to manifest at $\boldsymbol{q} \simeq \boldsymbol{k}_{W2'}$. In particular, the dynamical correlation almost exactly reproduces the strong phonon softening feature at Weyl node $\boldsymbol{k}_{W2'}$: with $v_F \sim 1.5 \times 10^5$ m/s in TaP and the momentum mismatch being $v_F \delta \boldsymbol{q} \sim 50$ meV, $\nu' \sim 60$ meV largely compensates for the mismatch down to $\sim$1%, thereby facilitating the satisfaction of the divergence condition and agreeing with the observation in Figs. 3(c)–3(f).

Chirality selection of the topological chiral Kohn anomaly.—The IXS measurements carried out near a W1 Weyl node [Fig. 4(a), and Fig. S9 in Ref. [21]] present a contrasting result. When the phonon $\boldsymbol{q}$ is near a W1 node $\boldsymbol{k}_{W1'} = (0.518, 0.014, 0)$, there is no clear indication of phonon softening at all measured temperatures, where measured phonon dispersions agree very well with *ab initio* calculations in Figs. 4(b)–4(e). This is largely due to the lack of a scattering channel that can simultaneously conserve momentum and chirality. For momentum-conserved scattering, although the phonon nesting condition can still roughly be met by considering scattering from $\boldsymbol{k}_{W2}$ to $\boldsymbol{k}_{W2'}$, where $\boldsymbol{q} = \boldsymbol{k}_{W2'} - \boldsymbol{k}_{W2} = (0.542, 0, 0) \approx \boldsymbol{k}_{W1'}$ (mismatch $|\boldsymbol{q} - \boldsymbol{k}_{W1'}|/|\boldsymbol{k}_{W1'}| \sim 5\%$) [Fig. 4(f)], the W2 and W2′ nodes have opposite chirality (+ and −, respectively), prohibiting the EPI to occur. On the other hand, for a chirality-conserved scattering $\boldsymbol{q} = \boldsymbol{k}_{W2'} - \boldsymbol{k}_{\overline{W2}}$, where $\boldsymbol{k}_{\overline{W2}} = (-0.271, -0.024, 0.578)$ gives the $\overline{\text{W2}}$ node paired with W2′ and has − chirality, the ∼8% momentum mismatch is simply too large to compensate even with dynamical effects considered. Moreover, the low carrier concentration of the hole pockets at W2 nodes further decreases the overall EPI contribution. As such, the magnitude of the Kohn anomaly at W1 should be imperceptible relative to the results at W2. This analysis corroborates the IXS data.

In addition to the two types of Weyl nodes, one may expect a Kohn anomaly to emerge at the Γ point. However, the chirality-conserved scattering channel (say, W1 and W1′) has large momentum mismatch away from the Γ point, while the momentum-conserved channel (say, W1′ and $\overline{\text{W1}}$) with $\boldsymbol{k}_{\overline{W1}} = (0.518, -0.014, 0)$ does not preserve chirality as shown in Figs. S11 [21]. A mixed behavior is observed from Raman scattering measurements. A weak

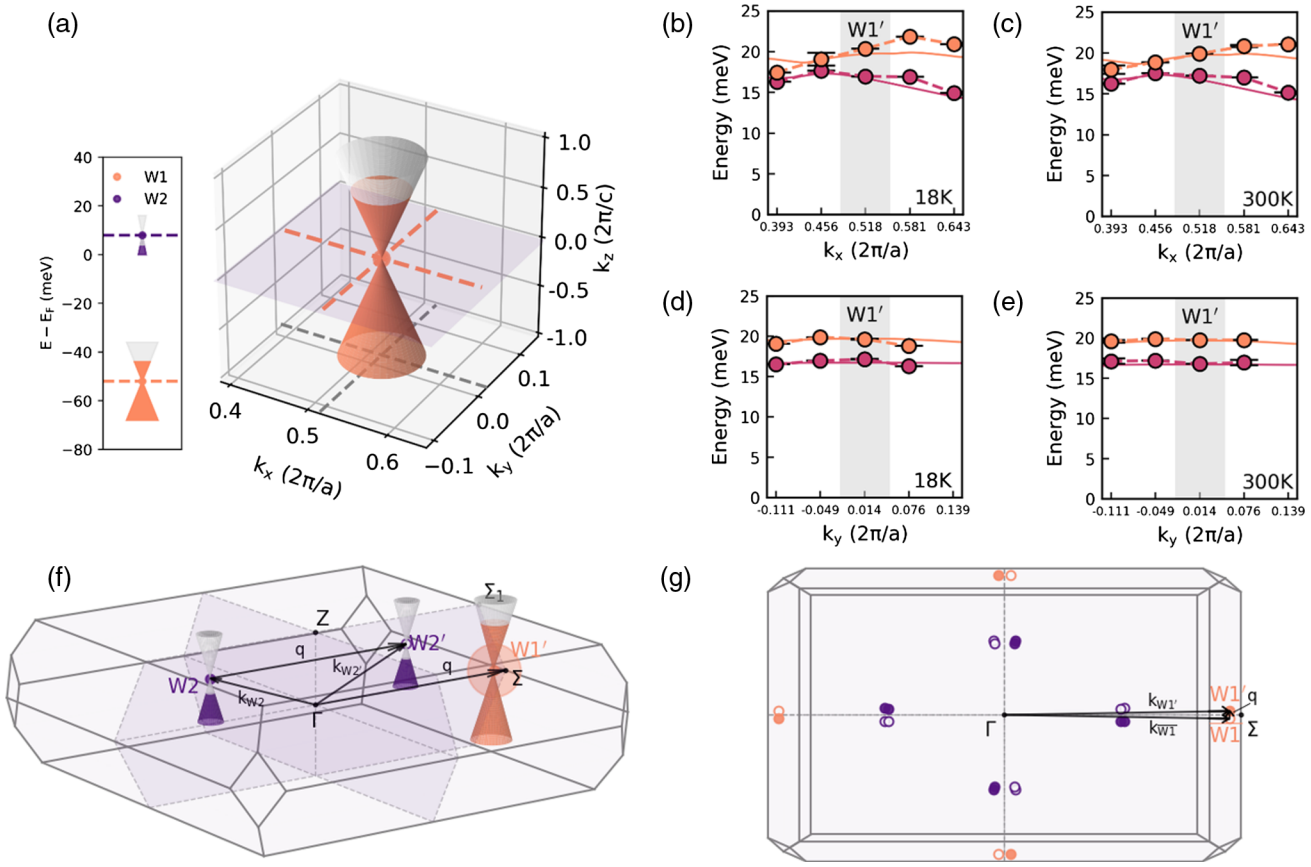

FIG. 4. Phonon characteristics at the W1 Weyl node and Γ-point. (a) Location of the W1 Weyl node in energy and momentum space. Dispersions of two representative phonon modes obtained from IXS data near W1 at (b), 18 and (c), 300 K along the k_x direction as well as (d) and (e), along the k_y direction. Error bars represent 1 standard deviation. Experimental phonon dispersion agrees excellently with *ab initio* calculations (solid lines). (f) Schematic of the connection of two equivalent electronic states at $\boldsymbol{k}_{W2}$ and $\boldsymbol{k}_{W2'}$ by the phonon $\boldsymbol{q} = \boldsymbol{k}_{W2'} - \boldsymbol{k}_{W2} \approx \boldsymbol{k}_{W1'}$, the W1 node near which IXS measurements were performed. (g) Schematic seen from the (001) plane of the connection between two equivalent electronic states at $\boldsymbol{k}_{W1'}$ and $\boldsymbol{k}_{\overline{W1}}$ by the phonon momentum $\boldsymbol{q} = \boldsymbol{k}_{W1'} - \boldsymbol{k}_{\overline{W1}} \approx \Gamma$.

softening ∼1.2 meV is observed for the lower optical phonon at the Γ point, but not for the higher-energy optical phonon. As a result, the intranode scattering may still happen and requires further investigation.

To summarize, we theoretically formulated and experimentally demonstrated a Kohn anomaly in a WSM, which can lead to the anomalous broad-range phonon softening behaviors arising from the scattering between the topological singularity of chiral Weyl nodes. Unlike a conventional Fermi liquid, in TaP, with 8 W1 nodes and 16 W2 nodes, numerous $\boldsymbol{q}$ regimes in the Brillouin zone can achieve Kohn anomalies. The recent *ab initio* calculations in Dirac semimetals also confirm the existence of Kohn anomalies in topological semimetals [39,40]. Moreover, in contrast to the conventional Fermi liquid with only static screening and logarithmic divergence $d\epsilon_r/dq \propto \ln(|q - 2k_F|/4k_F)$, or graphene and 2D electron gas with $\partial\epsilon_r/\partial q \propto 1/\sqrt{q^2 - 4k_F^2}$, we find a highly distinct divergence condition at $v_F q' \to \pm\nu'$ with a leading term $\partial\epsilon_r/\partial q \propto (v_F q')^3/[(v_F q')^2 - \nu'^2]$, where dynamical effects play a critical role with explicit Weyl node location dependence and chirality selection. The Kohn anomaly identified in our work highlights a previously overlooked instance of EPI in WSMs, and can offer a ubiquitous tool to extract the EPI strength, as carried out in graphite [41], to elucidate the interplay between chiral Weyl fermions and phonons. Our discovery adds to the rich array of exotic EPI effects realized in novel topological materials.

The authors thank S. Y. Xu for the helpful discussions. T. N. thanks the support from the MIT SMA-2 Fellowship Program and MIT Sow-Hsin Chen Fellowship. N. A. acknowledges the support of the National Science Foundation Graduate Research Fellowship Program under Grant No. 1122374. R. P. P. thanks the support from Fomento Económico Mexicano (FEMSA) and ITESM. A. A. thanks the support of MIT John Reed fund. Y. T. and Z. D. thank for the support from DOD Defense Advanced Research Projects Agency (DARPA) Materials for Transduction (MATRIX) program under Grant No. HR0011-16-2-0041. D. A. T. was sponsored by the Laboratory Directed Research and Development Program (LDRD) of Oak Ridge National Laboratory, managed by

UT-Battelle, LLC, for the U.S. Department of Energy (Project No. 9533). This research used resources of the Advanced Photon Source, a U.S. Department of Energy (DOE) Office of Science User Facility operated for the DOE Office of Science by Argonne National Laboratory under Contract No. DE-AC02-06CH11357. This research on neutron scattering used neutron research facilities at the High Flux Isotope Reactor, a DOE Office of Science User Facility operated by the Oak Ridge National Laboratory and at the NIST Center for Neutron Research (NCNR), at the National Institute of Standards and Technology, an agency of the U.S. Department of Commerce. The identification of any commercial product or trade name does not imply endorsement or recommendation by the National Institute of Standards and Technology. M. L. acknowledges the neutron sample alignment support from MIT Nuclear Reactor Laboratory Seed Fund Program. T. N., N. A., F. H. and M. L. acknowledge the support from the U.S. Department of Energy (DOE), Office of Science (SC), Basic Energy Sciences (BES), Award No. DE-SC0020148.

*These authors contributed equally to this work.
†Corresponding author.
mingda@mit.edu

[1] W. Kohn, Phys. Rev. Lett. **2**, 393 (1959).
[2] P. Aynajian, T. Keller, L. Boeri, S. M. Shapiro, K. Habicht, and B. Keimer, Science **319**, 1509 (2008).
[3] W. Weber, Phys. Rev. Lett. **58**, 1371 (1987).
[4] D. Reznik, L. Pintschovius, M. Ito, S. Iikubo, M. Sato, H. Goka, M. Fujita, K. Yamada, G. D. Gu, and J. M. Tranquada, Nature (London) **440**, 1170 (2006).
[5] S. Piscanec, M. Lazzeri, J. Robertson, A. C. Ferrari, and F. Mauri, Phys. Rev. B **75**, 035427 (2007).
[6] D. L. Mafra, L. M. Malard, S. K. Doorn, H. Htoon, J. Nilsson, A. H. Castro Neto, and M. A. Pimenta, Phys. Rev. B **80**, 241414(R) (2009).
[7] W.-K. Tse, Ben Yu-Kuang Hu, and S. Das Sarma, Phys. Rev. Lett. **101**, 066401 (2008).
[8] B. Wunsch, T. Stauber, F. Sols, and F. Guinea, New J. Phys. **8**, 318 (2006).
[9] A. C. Ferrari, Solid State Commun. **143**, 47 (2007).
[10] B. Renker, H. Rietschel, L. Pintschovius, W. Gläser, P. Brüesch, D. Kuse, and M. J. Rice, Phys. Rev. Lett. **30**, 1144 (1973).
[11] X. Zhu, L. Santos, C. Howard, R. Sankar, F. C. Chou, C. Chamon, and M. El-Batanouny, Phys. Rev. Lett. **108**, 185501 (2012).
[12] S.-Y. Xu *et al.*, Science **349**, 613 (2015).
[13] B. Q. Lv, N. Xu, H. M. Weng, J. Z. Ma, P. Richard, X. C. Huang, L. X. Zhao, G. F. Chen, C. E. Matt, F. Bisti, V. N. Strocov, J. Mesot, Z. Fang, X. Dai, T. Qian, M. Shi, and H. Ding, Nat. Phys. **11**, 724 (2015).
[14] H. Weng, C. Fang, Z. Fang, B. A. Bernevig, and X. Dai, Phys. Rev. X **5**, 011029 (2015).
[15] S.-M. Huang, S.-Y. Xu, I. Belopolski, C.-C. Lee, G. Chang, B. Wang, N. Alidoust, G. Bian, M. Neupane, C. Zhang, S. Jia, A. Bansil, H. Lin, and M. Z. Hasan, Nat. Commun. **6**, 1 (2015).
[16] C.-H. Min, H. Bentmann, J. N. Neu, P. Eck, S. Moser, T. Figgemeier, M. Ünzelmann, K. Kissner, P. Lutz, R. J. Koch, C. Jozwiak, A. Bostwick, E. Rotenberg, R. Thomale, G. Sangiovanni, T. Siegrist, D. Di Sante, and F. Reinert, Phys. Rev. Lett. **122**, 116402 (2019).
[17] A. Cortijo, Y. Ferreirós, K. Landsteiner, and M. A. H. Vozmediano, Phys. Rev. Lett. **115**, 177202 (2015).
[18] Z. Song, J. Zhao, Z. Fang, and X. Dai, Phys. Rev. B **94**, 214306 (2016).
[19] P. Rinkel, P. L. S. Lopes, and I. Garate, Phys. Rev. Lett. **119**, 107401 (2017).
[20] E. H. Hwang and S. Das Sarma, Phys. Rev. Lett. **101**, 156802 (2008).
[21] See Supplemental Material at http://link.aps.org/supplemental/10.1103/PhysRevLett.124.236401 for the complete derivation of the polarization and dielectric functions, which includes Refs. [22–27]; for details on the single crystal growth, the x-ray and neutron scattering experiments, and the data analysis, which includes Refs. [28–33]; and for details on the computational calculations, which includes Refs. [34–38].
[22] J. I. Kapusta and C. Gale, *Finite-Temperature Field Theory: Principles and Applications*, 2nd ed. (Cambridge University Press, New York, 2006).
[23] J. D. Bjorken, S. D. Drell, and P. B. Kahn, Am. J. Phys. **34**, 367 (1966).
[24] M. Lv and S.-C. Zhang, Int. J. Mod. Phys. B **27**, 1350177 (2013).
[25] J. Zhou, H.-R. Chang, and D. Xiao, Phys. Rev. B **91**, 035114 (2015).
[26] A. Thakur, K. Sadhukhan, and A. Agarwal, Phys. Rev. B **97**, 035403 (2018).
[27] K. Sadhukhan, A. Politano, and A. Agarwal, Phys. Rev. Lett. **124**, 046803 (2020).
[28] F. Han, N. Andrejevic, T. Nguyen, V. Kozii, Q. Nguyen, Z. Ding, R. Pablo-Pedro, S. Parjan, B. Skinner, A. Alatas, E. Alp, S. Chi, J. Fernandez-Baca, S. Huang, L. Fu, and M. Li, arXiv:1904.03179.
[29] H. Sinn, E. E. Alp, A. Alatas, J. Barraza, G. Bortel, E. Burkel, D. Shu, W. Sturhahn, J. P. Sutter, T. S. Toellner, and J. Zhao, Nucl. Instrum. Methods Phys. Res., Sect. A **467–468**, 1545 (2001).
[30] A. Alatas, B. M. Leu, J. Zhao, H. Yavas, T. S. Toellner, and E. E. Alp, Nucl. Instrum. Methods Phys. Res., Sect. A **649**, 166 (2011).
[31] T. S. Toellner, A. Alatas, and A. H. Said, J. Synchrotron Radiat. **18**, 605 (2011).
[32] J. W. Lynn, Y. Chen, S. Chang, Y. Zhao, S. Chi, W. Ratcliff, B. G. Ueland, and R. W. Erwin, J. Res. Natl. Inst. Standards Technol. **117**, 61 (2012).
[33] R. T. Azuah, L. R. Kneller, Y. Qiu, P. L. W. Tregenna-Piggott, C. M. Brown, J. R. D. Copley, and R. M. Dimeo, J. Res. Natl. Inst. Standards Technol. **114**, 341 (2009).
[34] G. Kresse and D. Joubert, Phys. Rev. B **59**, 1758 (1999).
[35] G. Kresse and J. Furthmüller, Comput. Mater. Sci. **6**, 15 (1996).
[36] G. Kresse, J. Furthmüller, and J. Hafner, Europhys. Lett. **32**, 729 (1995).
[37] J. P. Perdew, K. Burke, and M. Ernzerhof, Phys. Rev. Lett. **77**, 3865 (1996).

[38] A. Togo and I. Tanaka, Scr. Mater. **108**, 1 (2015).
[39] S. Yue, H. T. Chorsi, M. Goyal, T. Schumann, R. Yang, T. Xu, B. Deng, S. Stemmer, J. A. Schuller, and B. Liao, Phys. Rev. Research **1**, 033101 (2019).
[40] S. Yue, B. Deng, Y. Liu, Y. Quan, R. Yang, and B. Liao, arXiv:2001.10124.
[41] S. Piscanec, M. Lazzeri, F. Mauri, A. C. Ferrari, and J. Robertson, Phys. Rev. Lett. **93**, 185503 (2004).